Performance Analysis of Tomographic Methods Against Experimental Contactless Multistatic Ground Penetrating Radar

Michele Ambrosanio ⬤, *Member, IEEE*, Martina Teresa Bevacqua ⬤, *Member, IEEE*, Tommaso Isernia ⬤, *Senior Member, IEEE*, and Vito Pascazio ⬤, *Senior Member, IEEE*

Abstract—Ground-penetrating radar (GPR) technology for underground exploration consists of the transmission of an electromagnetic signal in the ground for sensing the presence of buried objects. While monostatic or bistatic configurations are usually adopted, a limited number of multistatic GPR systems have been proposed in the scientific literature. In this article, we investigate the recovery performance of a specific and unconventional contactless multistatic GPR system, designed at the Georgia Institute of Technology for the subsurface imaging of antitank and antipersonnel plastic mines. In particular, for the first time, tomographic approaches are tested against this experimental multistatic GPR system, while most GPR processing in the scientific literature processes multimonostatic experimental data sets. First, by mimicking the system at hand, an accurate theoretical as well as numerical analysis is performed in order to estimate the data information content and the performance achievable. Two different tomographic linear approaches are adopted, i.e., the linear sampling method and the Born approximation (BA) method, this latter enhanced by means of the compressive sensing (CS) theoretical framework. Then, the experimental data provided by the Georgia Institute of Technology are processed by means of a multifrequency CS- and BA-based method, thus generating very accurate 3D maps of the investigated underground scenario.

Index Terms—Born approximation (BA), compressive sensing (CS), ground-penetrating radar (GPR), inverse scattering (IS) problem, linear sampling method (LSM), microwave tomography, plastic landmine detection, sparse recovery.

I. INTRODUCTION

GROUND-PENETRATING radar (GPR) represents a powerful technology able to investigate in a noninvasive

Michele Ambrosanio and Vito Pascazio are with the Dipartimento di Ingegneria, Università degli Studi di Napoli "Parthenope," Centro Direzionale di Napoli, 80143 Napoli, Italy (e-mail: michele.ambrosanio@uniparthenope.it; vito.pascazio@uniparthenope.it).

Martina Teresa Bevacqua and Tommaso Isernia are with the Consorzio Nazionale Interuniversitario per le Telecomunicazioni (CNIT) Viale G.P. Usberti, 43124 Parma, Italy, and with the DIIES, Department of Information Engineering, Infrastructures and Sustainable Energy, Università Mediterranea di Reggio Calabria, 89124 Reggio di Calabria, Italy, and with the Institute for Electromagnetic Sensing of the Environment, National Research Council of Italy, 80124 Naples, Italy, and also with the Consorzio Nazionale Interuniversitario per le Telecomunicazioni (CNIT) Viale G.P. Usberti, 43124 Parma, Italy (e-mail: martina.bevacqua@unirc.it; tommaso.isernia@unirc.it).

Digital Object Identifier 10.1109/JSTARS.2020.3034996

and nondestructive way nonaccessible scenarios, as witnessed by the numerous and different applications, which include demining, lunar explorations, archaeology, geology, and civil engineering [1].

GPR technology is usually adopted for subsurface imaging and is based on the transmission of an electromagnetic signal in the ground and the measurement of the returning signal. Several GPR systems have been introduced in the literature. In early systems, the antennas are operated in contact with the investigated scenario. Later these systems were designed to work at a stand-off distance from the air-scenario interface and named contactless ones [2]–[4]. Most of them are based on monostatic or bistatic configurations. These two simple configurations do not allow one to collect detailed information on the subsurface and requires an expert user's interpretation [1].

For this reason, GPR systems with multichannel and/or antenna array configurations have been proposed to collect a larger amount of data. Differently from monostatic or bistatic systems, multistatic systems are not so common [5]–[7]. They usually involve more complex hardware, but they allow us to collect more information on the targets hosted in the investigated scenario by exploiting different angular perspectives, not allowed by monostatic or fixed bistatic systems.

Recently, a particular contactless multistatic GPR system [8] consisting of a linear array of eight resistive-vee antennas has been developed at the Georgia Tech (GT) Institute for subsurface imaging of anti-tank and anti-personnel plastic mines buried in different environments. The data produced by this GPR system have been made available online and proposed as a benchmark to prove the efficiency of inversion algorithms for GPR surveys.

Different researchers have processed this multistatic data set [9]–[12]. All these methods belong to deconvolution-based approaches, wherein one essentially processes the GPR data without modeling the underlying scattering phenomena.

In this article, to the best of authors' knowledge, for the first time, tomographic approaches [13], [14] are tested against the multistatic GT GPR system [8]. Conversely from radar-based ones, these techniques take into account the scattering phenomena and the interactions between the electromagnetic signal and the buried objects. More in detail, the novelty of this work is related to the preprocessing, rearrangement, and processing of data collected by this unconventional GPR system located at a stand-off distance from the soil. These aspects are

not trivial since the data arrangement of this kind of system is very peculiar and it is different from other systems available in the research community which usually exploit multimonostatic and/or full-aperture configurations.

First, a theoretical as well as numerical analysis is performed by exactly mimicking the GT GPR system [8], in order to qualify and quantify the data information content, in comparison with the case of full multistatic array aperture, that is an array having the same size as the transverse dimension of the scanned domain. To this aim, starting from the results in [15], an energy indicator is introduced, which allows one to *a priori* evaluate the reconstruction capabilities of the inversion approach as a function of the array aperture. Moreover, in the same line of reasoning, the spectral coverage is evaluated [16].

Second, a "controlled" assessment with simulated data is carried out in a bidimensional geometry by adopting two popular tomographic approaches that are the linear sampling method (LSM) [17], [18] and the Born approximation (BA) [19]. Both approaches are characterized by a simple mathematical model and low computational burden but require an adequate amount of information. To partially counteract the difficulty of working under aspect-limited measurement configurations, a multifrequency processing and a regularization technique based on the theory of compressive sensing (CS) [20] have been adopted. In particular, the sparsity requirement, enforced by means of an iterative shrinkage thresholding algorithm [21], [22], has allowed to improve the resolution and accuracy of BA reconstructions. This analysis is useful in order to understand the role of multifrequency processing and identify the more suitable processing method.

Finally, the multifrequency BA method enhanced by sparsity regularization is tested against the experimental data collected by the GT GPR system, which are properly rearranged and filtered, in order to handle the clutter, by using both the time gating as well as the background removal. Reliable reconstructions via a 2.5D inversion procedure are then obtained. This latter consists of a 2D processing starting from a 3D data collection. Then, each reconstructed 2D slice is merged with the others to obtain a 3D rendering of the investigated area [23], [24].

The article is organized as follows. In Section II, the discretized version of the equations modeling inverse scattering problem underlying tomographic approaches is reported. Section III introduces the basics underlying BA and LSM for the half-space case. In Sections IV, the multistatic GPR system in [8] is briefly recalled and analyzed to *a priori* qualify and quantify the amount of collected information. Section V is focused on a "controlled" assessment of both LSM and BA in order to understand the optimal achievable performance, while in Section VI the experimental imaging reconstructions of plastic pipe, anti-tank, and anti-personnel plastic mines buried in the sand are reported. Conclusions follow.

II. MATHEMATICAL MODEL OF THE INVERSE SCATTERING PROBLEM UNDERLYING GPR IMAGING

Let us assume and drop the time harmonic factor $\exp\{j\omega t\}$. The scenario under investigation, depicted in Fig. 1, is supposed to be composed of two nonmagnetic media: the first medium
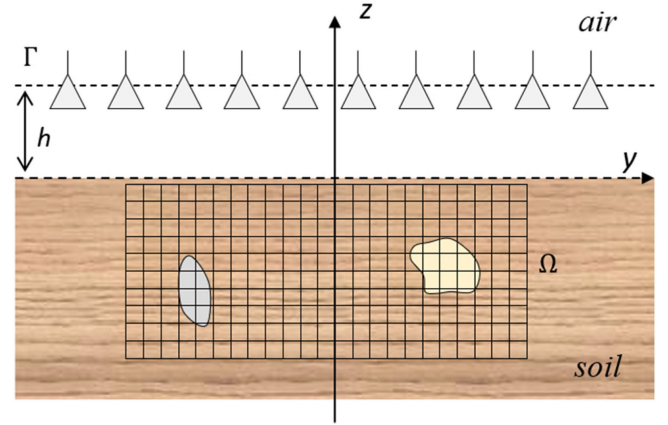

Fig. 1.   Sketch of a MVMS GPR system.

with electromagnetic properties of the air, the second medium with electromagnetic features $\varepsilon_b(\underline{r},\omega)$ and $\sigma_b(\underline{r},\omega)$, wherein some unknown targets are supposed to be embedded (being $\underline{r} = (y,z) \in \Omega$ the generic coordinate of the reference system yz, $\omega = 2\pi f$ and f the working frequency.)

The investigation domain Ω in the second medium is supposed to be probed by means of a linear antenna array located in the air at a given height h from the air-soil interface, composed of some antennas acting as receivers (whose number is N_R) and some others acting as transmitters (whose number is N_T) located on a measurement line Γ. The data are supposed to be collected under a multiview-multistatic (MVMS) measurement configuration, i.e., one transmitter per time is active meanwhile all the receivers sample the scattered signal. Under the above, the two fundamental equations modeling the relevant scattering problem are the data and the state equations. After a proper discretization of Ω in $N_P = N_Z \times N_Y$ pixels and of the frequency domain in N_F frequencies, the scattering equations become

$$\boldsymbol{e}_t = \boldsymbol{e}_i + \mathbf{A}_i\left(\boldsymbol{x} \odot \boldsymbol{e}_t\right) \tag{1.a}$$

$$\boldsymbol{e}_s = \mathbf{A}_e\left(\boldsymbol{x} \odot \boldsymbol{e}_t\right) \tag{1.b}$$

where the elements of the $1 \times (N_P \times N_F)$ vector $\boldsymbol{x}$ represent the unknown contrast, $\boldsymbol{e}_i$ and $\boldsymbol{e}_t$ are the $1 \times (N_P \times N_T \times N_F)$ vectors which sample the incident known field and the total unknown field, respectively, $\boldsymbol{e}_s$ is the $1 \times (N_R \times N_T \times N_F)$ vector which samples the scattered electric field measured on Γ. $\mathbf{A}_i$ and $\mathbf{A}_e$ are the discrete counterparts of integral operators for the half-space case, involving the Sommerfeld–Green functions [25]. The operation "$\odot$" denotes the element-by-element product.

The inverse scattering problem at hand aims at retrieving the unknown contrast $\boldsymbol{x}$ from the scattered field $\boldsymbol{e}_s$ measured with a finite number N_R of receivers on Γ, when a finite number N_T of transmitters is considered. Such a problem is both nonlinear, as the total field depends on the unknown contrast function, and ill-posed, due to the compactness of the external radiation operator [26]. In GPR inspections, these difficulties are further worsened as the useful data are collected under an aspect-limited measurement configuration [27].

III. TOMOGRAPHIC METHODS

In the following, we are dealing with the subsurface target detection. To this end, both the LSM and BA are considered.

A. Linear Sampling Method

Among qualitative methods, the LSM is probably one of the most popular. It achieves the support information in a simple and effective way by solving for a fixed frequency and point of the $N_Z \times N_Y$ grid, the well-known far-field equation (FFE) [15], [17], [18]

$$\boldsymbol{F}\boldsymbol{\alpha} = \boldsymbol{g}_e \tag{2}$$

wherein $\boldsymbol{\alpha}$ represents the $N_T \times 1$ unknown vector, $\boldsymbol{g}_e$ is the $N_R \times 1$ vector containing the values of the field measured on Γ when an elementary current is located in the considered point of the grid, and the presence of the interface is taken into account. Finally, $\boldsymbol{F}$ is a $N_R \times N_T$ matrix whose generic element is the scattered field $\boldsymbol{e}_s$ at the given frequency.

The problem in (2) is linear; however, it is ill-posed and requires the adoption of a regularization technique. In the following, the Tikhonov regularization is considered following the guidelines in [18]. Then, the target support is estimated by computing $\boldsymbol{\alpha}$ in each point of the grid at the considered frequency, and by plotting its energy, that is

$$\Im_{LSM} = \frac{\|\boldsymbol{\alpha}\|_2^2}{\|\boldsymbol{g}_e\|_2^2} \tag{3}$$

wherein $\| \cdot \|_2$ is the l_2-norm and $\Im_{\text{LSM}}$ is a $N_Z \times N_Y$ matrix, which is referred as LSM indicator. In the above definition, the energy of $\boldsymbol{\alpha}$ is normalized to the energy of the known term of the FFE (3), as subsurface imaging is dealt with [18].

In subsurface inspection, the scattered data can be collected only in reflection mode. In order to improve the quality of the achieved map, the LSM can take advantage of using multifrequency data, as described in [18].

B. Born Approximation Method

The BA [19] belongs to approximated methods and solves the inverse scattering problem by means of a convenient linearization of the discretized data (1.b), that is

$$\boldsymbol{e}_s = \boldsymbol{L}(\boldsymbol{x}) + \boldsymbol{n} \tag{4}$$

wherein $\boldsymbol{L}(\cdot) = \mathbf{A}_e(\cdot \odot \boldsymbol{e}_i)$ and $\boldsymbol{n}$ is the unavoidable additive measurement noise. It is worth to note that the operator $\mathbf{A}_e$ models the air-soil interface.

The problem in (4) is ill-posed and requires the adoption of a regularization technique. In order to restore the well-posedness of the problem, in the following, we consider both the truncated singular value decomposition (TSVD) [26] and CS framework [20]. In particular, as far as CS is concerned, an approach based on the class of iterative shrinkage thresholding algorithms (ISTA) is adopted, wherein a shrinkage/soft-threshold step is involved [21], [22].

The approximation adopted in (4) is fully satisfied only in the case of weak scatterers and/or for objects whose dimension is
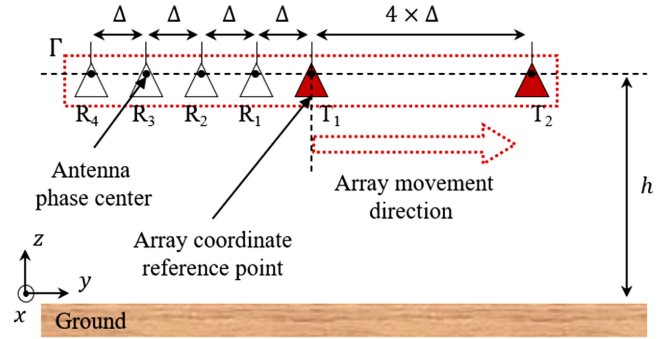

Fig. 2. GT GPR system. The spacing between contiguous receivers is $\Delta = 12$ cm and the height from the ground is $h = 27.8$ cm.

very small in terms of the wavelength in the external medium. In other cases, BA can be used for their localization.

In this particular case, in order to improve the imaging quality and the estimation of the target support, one can assume the unknown $\boldsymbol{x}$ constant with respect to the frequency. As such, BA has the unique advantage of simultaneously processing the multifrequency data, without adopting a dispersion law and, unlike LSM, without requiring a posteriori combination of the single-frequency results. This approach is robust with respect to the data noise and the limited amount of available data, as shown in Section V.

IV. GT MULTISTATIC GPR DATA SET: DATA ARRANGEMENT AND INFORMATION CONTENT

The multistatic GPR system developed at the Georgia Institute of Technology is based on the use of a linear array of resistive-vee antennas [28]. The system is composed of two transmitters and four receivers arranged as in Fig. 2. Each pair of contiguous receivers (R_1–R_2, R_2–R_3, R_3–R_4) is 12-cm spaced, while the two transmitters (T_1–T_2) are located at a 48-cm distance from each other. Thus, this arrangement of the antennas provides eight bistatic pairs spacing from 12 to 96 cm in 12-cm increments.

The GPR scanned area extends for a 1.8×1.8 m^2 region with the scanning system located above the surface of the ground at a constant height of 27.8 cm. The linear array of transmitters and receivers moves above the investigated area in a stepped fashion with a spatial sampling step of 2 cm. Thus, the investigated surface is discretized into a grid of 91 points by 91 points. Each time the array stops in a location, it collects data from the eight bistatic pairs by means of 401 equally spaced frequency points from 60 MHz to 8.06 GHz (i.e., a frequency step equal to 20 MHz). After collection, the data are calibrated and stored (more details regarding the data calibration are reported in [8]). Note that, as far as the GPR perspective is concerned, the highest frequencies in the employed 8-GHz bandwidth are not reliable due to the attenuation in the soil, while this bandwidth is efficient for the air-target test case [29].
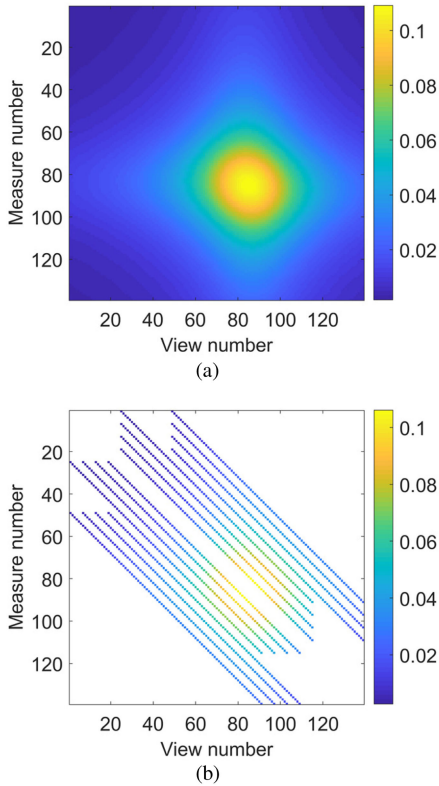
Fig. 3.   Matrix arrangement collected by MVMS GPR systems: (a) full aperture array and (b) moving array as in GT GPR system. Different from (a), (b) is a diagonally striped matrix. For details about data simulation, the readers are referred to Section V.

A. Diagonally Striped MVMS Scattering Matrix

The data arrangement of the GT systems is very peculiar and it is different from other systems available in the research community which usually exploit multi-monostatic and/or full-aperture configurations.

Notably, in tomographic approaches, the data vector e_s can be re-arranged for a fixed frequency in a $N_R \times N_T$ matrix wherein the generic entry (i, j) is the complex scattered field value at the ith receiver for the jth transmitter position. Due to the reciprocity of the medium, the filled matrix is symmetric.

In case of array aperture equal to the transversal dimension of the scanned area, the data matrix is dense [see Fig. 3(a)]. This measurement configuration represents the "optimal" case wherein all the Tx-Rx pair measurements are available. In the following, we refer to it as the full aperture configuration.

However, with the aim of reducing as much as possible the complexity and cost of the measurement set-up as well as the processing computational burden, an array with an aperture smaller (as well as a smaller number of antennas) than the transversal extent of the scanned area is usually adopted and the data are collected by moving the array. In such a case, the elements of the MVMS data matrix corresponding to transmitter–receiver pairs for which the scattered field is not measured are not available and simply replaced with zeroes [15].

Conversely from the full aperture configuration, which is well-known in the tomographic imaging community [30]–[35],

in the GT MVMS system, for each slice scanning and each rigid translation of the array along y, only eight view-measure pairs are collected. This results in the scattering matrix as shown in Fig. 3(b). In particular, the peculiarity of the Tx-Rx pairs (see Fig. 2) is responsible for a dominant diagonally striped behavior of the MVMS scattering matrix. Indeed, the matrix consists of nonzero diagonal elements such that adjacent diagonals of at least one nonzero diagonal are zero. Moreover, each nonzero diagonal corresponds to a specific Tx-Rx pair. Finally, the lower triangular block of the data matrix is properly filled by exploiting reciprocity of the medium involved in the analysis.

By comparing the two data matrices in Fig. 3, it is clear that the amount of data collected with the GT GPR system is limited with respect to the case of full aperture array. A natural question, then, arises concerning the impact of this aspect-limitedness at hand on the recovery performance.

B. Expected Performance Indicator for GPR System

It is quite trivial to note that the recovery performance depends not only on GPR data processing but also on the measurement configuration involved in the scanning [13], [16].

Inspired by the work [15], in this section, a qualitative performance indicator is proposed and evaluated for the considered GPR system. In order to evaluate this indicator, two quantities are dealt with, i.e., the *probing wave footprint* "$\mathcal{T}$" and the *sampling point footprint* "$\mathcal{R}$," which represent the region wherein the array is able to radiate a significant energy and the capability of an elementary source located in a point of the imaging domain to radiate a significant field at the receivers, respectively.

The probing wave footprint is related to the energy of the incident field e_i radiated by the considered N_T antennas located on Γ, in every point of the $N_Z \times N_Y$ imaging domain grid, i.e., (at a fixed frequency and in its discrete form)

$$\mathcal{T} = \|e_i\|_\Gamma^2 \qquad (5)$$

with $\|(\cdot)\|_\Gamma$ being the l_2-norm on Γ and $\mathcal{T}$ a $N_Z \times N_Y$ matrix. In short, this quantity is related to the energy of the field radiated in the imaging domain by considering all the transmitters acting together. Conversely, the sampling point footprint is related to the energy of the field radiated e_{rx} by an elementary source located in each of the $N_Z \times N_Y$ sampling points of the imaging domain and observed at the N_R receivers on Γ, thus,

$$\mathcal{R} = \|e_{rx}\|_\Gamma^2 \qquad (6)$$

with $\mathcal{R}$ being a $N_Z \times N_Y$ matrix. Nevertheless, tomographic GPR surveys usually exploit linear arrays smaller than the extension of the investigated area, as for the experimental GPR setup at hand. Therefore, the quantities introduced previously can consider the case of a moving array. By doing so, it is possible to define an expected performance indicator to appraise the imaging capability achievable

$$\mathcal{J} = 10 \cdot \log_{10} \left[\frac{\tilde{\mathcal{T}} \cdot \tilde{\mathcal{R}}}{\max \left[\tilde{\mathcal{T}} \cdot \tilde{\mathcal{R}} \right]} \right]^{\frac{1}{2}} \qquad (7)$$
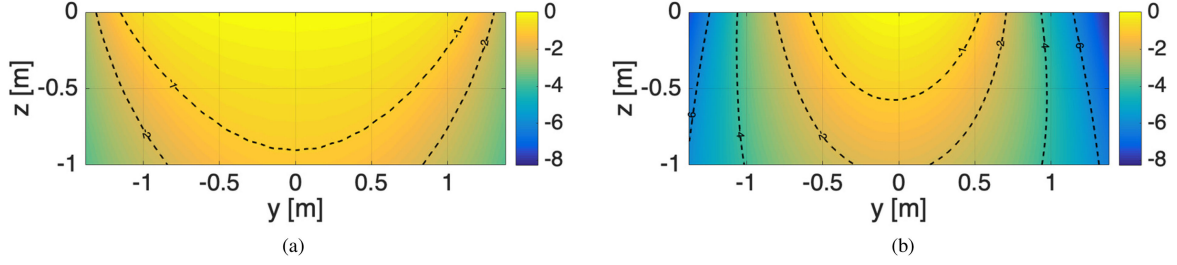
Fig. 4. Expected GPR performance indicator $\mathcal{J}$ as defined in (7) for the standard full aperture MVMS system (a) and for the experimental GT GPR system (b). They correspond to the data collections reported in Fig. 3(a) and (b), respectively.
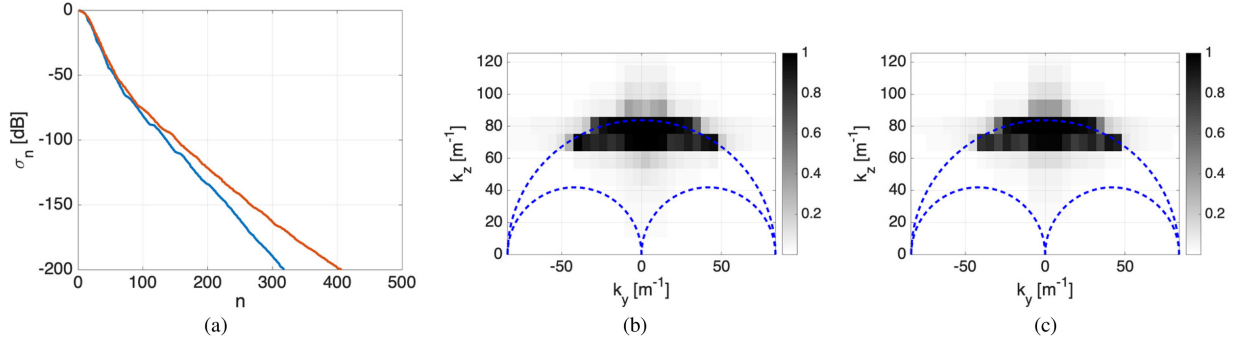

Fig. 5. Normalized singular values (a): full aperture MVMS system (red line) and the experimental GT GPR system (blue line). Spectral coverage analysis: (b) full aperture MVMS system and (c) the experimental GT GPR system. The variables (k_y, k_z) are the spatial frequency variables corresponding to the spatial coordinates (y, z), (i.e., lateral and depth coordinates, respectively) in the Fourier domain.

where $\max$ is the maximum of its argument evaluated with respect to the grid of $N_Z \times N_Y$ points, and

$$\tilde{\mathcal{T}} = \sum_{k=1}^{K} \|e_i^{(k)}\|_\Gamma^2$$

$$\tilde{\mathcal{R}} = \sum_{k=1}^{K} \|e_{rx}^{(k)}\|_\Gamma^2 \qquad (8)$$

with $e_i^{(k)}$ and $e_{rx}^{(k)}$ corresponding to the kth array position, and K defining the total number of array positions scanning the area. It is worth to note that the same number of transmitters and receivers for each array position is assumed, dealing with rigid translations. However, (7) is still valid for nonmoving array configurations, in which case (8) coincide with (5) and (6).

Fig. 4 reports the expected performance indicators defined in (7) for the full aperture configuration and for a system mimicking the GT MVMS GPR system.[1] It is quite evident that the adoption of this latter setup limits the extension of the investigated area reached by the highest amount of energy both in the y and z axes with respect to the case of full-aperture configuration. This means that objects buried in the deeper and sider parts of the investigation area could be not properly imaged. In order to overcome these limitations, the use of multifrequency data can be paramount, as shown in Section V.

In order to further understand if the GPR system at hand allows us to achieve good recovery performance which is comparable

with the optimal case of full-aperture configuration, the amount of retrievable independent information is evaluated and, thus, the spectral content of the tomographic imaging operator is analyzed. This spectral content quantifies the set of retrievable spatial harmonic components of a buried target, also known as spectral coverage of the operator [16]. To this aim, by considering the single-frequency measurement configuration and the linear model arising from BA, the spectral contents for both configurations have been evaluated via singular value decomposition. The obtained spectral coverages are reported in Fig. 5 both in the case of full and GT GPR configurations. Fig. 5 underlines that no difference in the classes of retrievable objects exists between the cases of full aperture and GT-like systems.

V. LSM AND BA METHODS AGAINST THE GT MVMS SYSTEM: NUMERICAL ANALYSIS

Before processing the experimental GT dataset, a "controlled" assessment with simulated data has been carried out in a 2D geometry to understand the achievable performance when LSM and BA are exploited. The reason for choosing these two well-known inversion approaches is related to their simple implementation and low computational burden as a test-case to show the proper handling and arrangement of the unconventional sampled data.

It is worth to note that a performance assessment of the well-known BA and LSM methods, whose resolution capabilities and recovery performance under model errors have been explored deeply in the research community, is out of the scope of this article. This latter is instead focused on the study of

[1]For details about data simulation, the readers are referred to Section V.
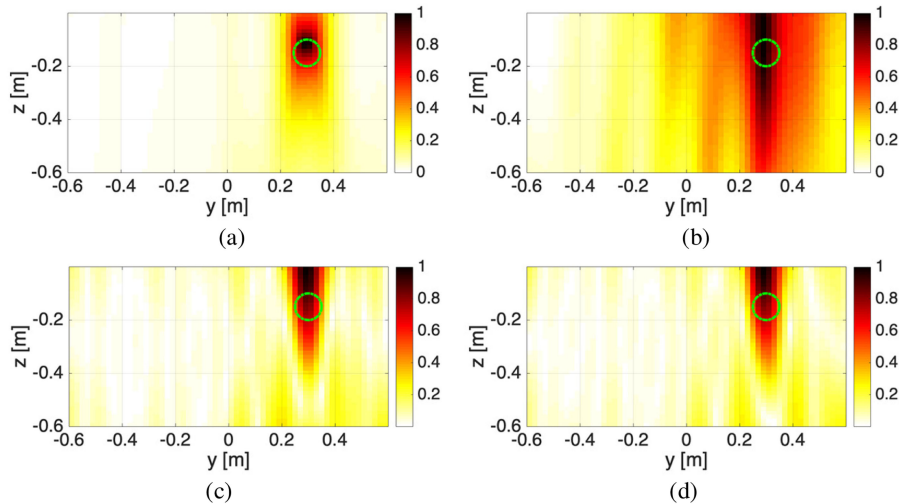
Fig. 6.   Single-frequency analysis: normalized LSM (a) and (b) and BA (c) and (d) indicators. Processing of full aperture (a) and (c) and GT GPR (b) and (d) systems. In both cases (c) and (d) the value of the adopted truncation index N_t is 30.

the recovery performance of the GT unconventional GPR system. Thus, all the numerical analyses reported in this section were thought to test and understand how to process these data properly.

The simulated scenario consists of a half-space sandy soil whose electromagnetic properties are $\varepsilon_b(\underline{r}) = 4$ and $\sigma_b(\underline{r}) = 1\,\text{mS/m}$. The soil embeds a circular metallic cylinder with a radius of 0.05 m and center located at $y = 0.30$ m and $z = -0.15$ m. The rectangular imaging domain is $1.2 \times 0.6\,\text{m}^2$ wide and has been discretized into 60×40 cells.

A linear array, with extension as long as the transversal dimension of the region scanned by the experimental GT system, consisting of $N = M = 139$ antennas, has been located at 0.278 m from the air–soil interface. The antennas are evenly spaced of 0.02 m and each one alternatively acts as a transmitter, while the other ones measure the corresponding scattered field. This latter has been simulated by means of a 2D full-wave finite element solver and corrupted by white Gaussian noise at an $\text{SNR} = 30$ dB. The thus obtained data correspond to full aperture configuration [see Fig. 3(a)]. In order to reproduce the GT system, the scattered data matrix has been organized in a 139×139 matrix and masked in such a way to extract just the data corresponding to actual Tx-Rx pairs [see Fig. 3(b)].

A comparison of the performance obtained by the full-aperture configuration and the GT-like system is performed. It is important to note that the processing of the full aperture data provides a benchmark, being the "optimal" possible result that can be achieved when subsurface imaging is dealt with by exploiting an array with the aperture equal to the extension of the scanned region.

In the following, as far as the regularization techniques are concerned, the truncation index N_t of the TSVD is determined by exploiting the Picard plot technique [36], [37] and its value is reported in the captions of the figures. While for the inversion performed via ISTA [38], the regularization parameter is selected ranging from 0.05 down to $5 \cdot 10^{-4}$.

Finally, in order to perform a fair comparison, both the LSM indicator and BA solution have been normalized. In particular, the BA solution has been normalized to its maximum value, while the LSM indicator has been rescaled as described in [30].

A. Single-Frequency Analysis

The data have been simulated at a working frequency of 1 GHz. The results achieved by using both LSM and BA are shown in Fig. 6. As can be seen, when a full configuration is considered, the LSM ensures the localization and detection of the target, see Fig. 6(a). However, the performance of LSM worsens when the GT GPR configuration is used. Indeed, if few receivers are adopted, the solution of FFE may not provide reliable images of the targets. In particular, the LSM is not able to correctly retrieve the target, especially its vertical size, see Fig. 6(b). Similar results can be observed in the case of BA, whose recovery performance seems stable enough with respect to data reduction [see Fig. 6(c) and (d)]. Indeed, in both cases, the obtained map is not suitable to estimate the support of the object at hand.

The following analysis shows that the amount of single-frequency data collected by means of the GT system allows to detect targets embedded in the soil, but it is not appropriate to correctly retrieve their supports. This circumstance holds true both in the case of LSM and BA.

B. Multifrequency Analysis

In order to counteract the limited amount of data and improve the accuracy of the reconstructions, multifrequency data have been processed. To this end, the range of the considered frequencies was [0.8, 2] GHz, with a frequency step of 40 MHz, for a total number of 31 frequencies.

In Fig. 7(a) and (b) the normalized LSM indicators, corresponding to both configurations of the scattered data matrix and 31 frequencies, are shown. As it can be seen, even if more
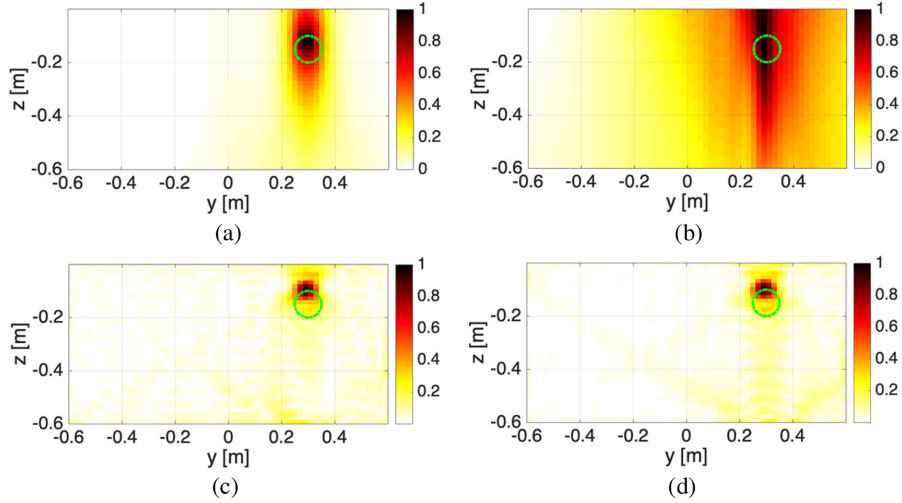
Fig. 7. Multifrequency analysis: normalized LSM ($N_F = 31$) (a), (b) and BA ($N_F = 8$) (c), (d) indicators. Processing of full aperture (a),(c) and GT GPR (b),(d) systems. Values of the truncation indices: $N_t = 300$ for (c) and $N_t = 135$ for (d).
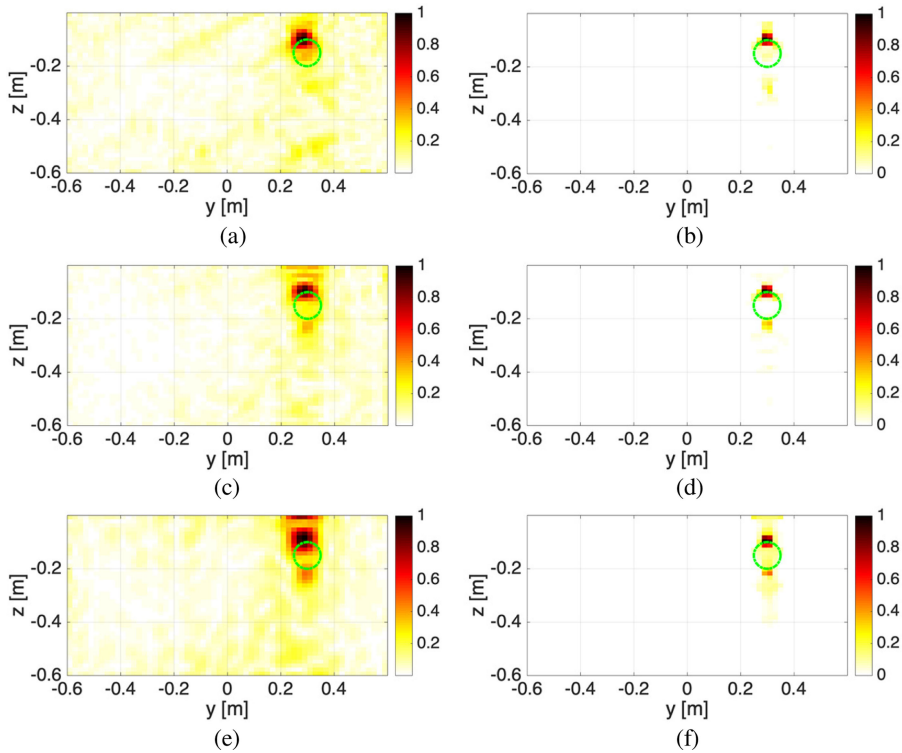

Fig. 8. Multifrequency analysis with TSVD (first column) and ISTA (second column). Reduction in the number of frequencies. $N_F = 4$ (a), (b), $N_F = 3$ (c), (d) and $N_F = 2$ (e), (f). Values of the truncation indices: $N_t = 300$ for (a), $N_t = 200$ for (c), and $N_t = 110$ for (e).

information has been processed, when LSM is adopted, this information is not enough to retrieve targets' support. This is due to the fact that multifrequency LSM involves an *a-posteriori* combination of the indicator maps related to each frequency.

On the other hand, BA is able to detect and correctly retrieve the shape of the circular metallic cylinder [see Fig. 7(c) and (d)]. The reason for which BA outperforms LSM is related to the way these approaches exploit the multifrequency information,

i.e., the BA uses all the frequencies simultaneously, while the LSM does not. This circumstance is also ensured when a reduced number of frequencies has been processed. In Fig. 8, the support reconstructions in the case of 4, 3, and 2 frequencies as well as TSVD and ISTA processing are reported. In particular, ISTA processing allows us to reach more accurate reconstructions, especially in case of a low number of frequencies. This is due to the capability of sparsity promotion to ensure good accuracy in
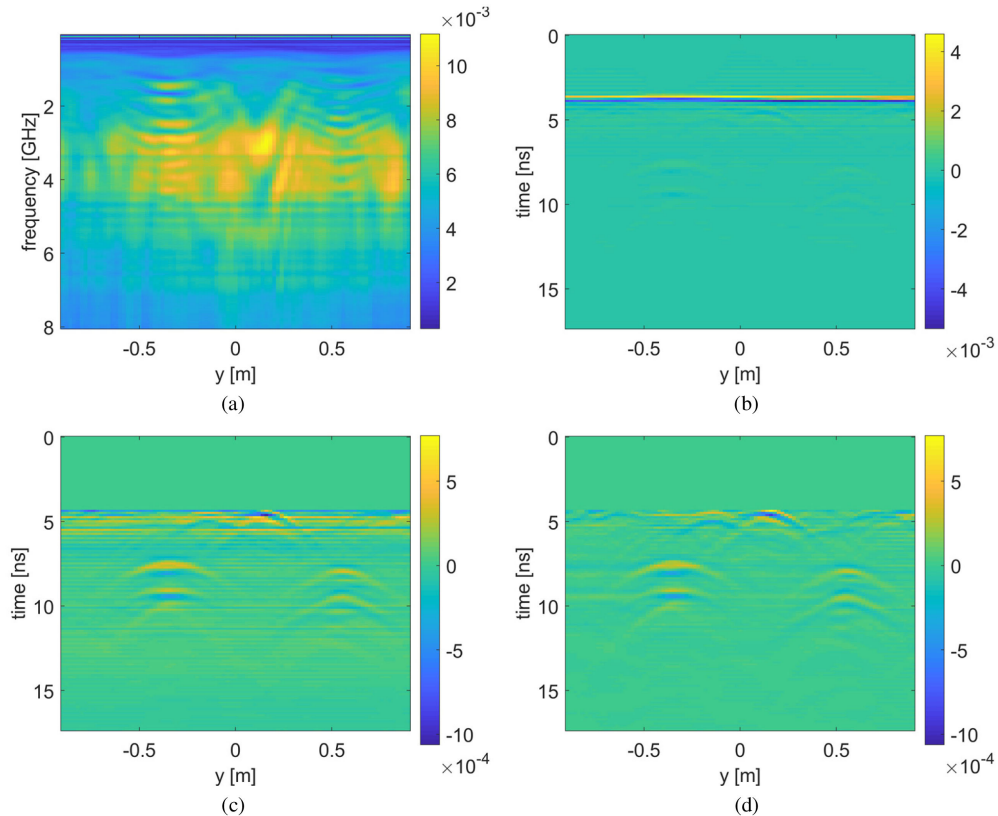
Fig. 9. Overview of experimental data preprocessing as described in Section VI-A. For the sake of clarity, the slice at $x = 0$ of the data set described in Section VI-B is reported as proof of concept. (a) Raw calibrated data, (b) raw radargram (time domain) in which the air–soil interface is clearly visible, (c) radargram after time gating (i.e., muting of the interface), and (d) radargram after time gating and background removal procedures.

case of few data. Regarding the number of transmitters/receivers, since a few transmitters and receivers were used (i.e., two transmitters and four receivers), we have not reduced further the number of data.

Due to the above results, in the following, we process the experimental GT data set by means of a multifrequency BA method, enhanced by ISTA. It is worth to note that the conclusions and analyses performed in this section are not strictly case-specific but allow to draw some general understandings for MVMS systems which operate in "reduced" measurement configurations similar to the GT one.

VI. EXPERIMENTAL SUBSURFACE IMAGING

In this section, the processing of the experimental GT data sets is proposed. The calibrated data have been made available by Prof. Waymond Scott at the Georgia Institute of Technology and stored in a MATLAB format [39].

A. Preprocessing of the Data

The calibrated data require a proper preprocessing step before running the tomographic imaging procedures. The ideal clutter removal procedure consists of subtracting from the total field the one due to the clutter sources. As a matter of fact, a key factor in clutter removal techniques is the muting of the air-soil interface, as well as the estimation of its roughness [40]–[43].

In the considered case, the involved processing can be summarized in the following main steps:

1) inverse Fourier transform to move to time domain;
2) muting of the air–soil interface by time gating;
3) removing spurious abrupt contributions and other sources of clutter via background removal; and
4) direct Fourier transform to move back to frequency domain.

An overview of the preprocessing steps applied for the mine data set (slice corresponding to abscissa $x = 0$), described in the following section, is reported in Fig. 9 as proof of concept.

First, the collected data are Fourier inverse-transformed to move to the time domain, obtaining the raw radargram. After that, a procedure to efficiently remove the echo coming up from the air-soil interface is required. This step represents one of the most challenging problems in GPR surveys, as it discriminates the field backscattered by the buried objects from the one reflected by medium interfaces as well as by targets located outside the imaging domain [44], [45].

Among the different strategies, a very simple filtering approach has been employed in the following, which is commonly referred to as time-gating (TG). In this approach, the problem is recast in terms of rays and the first received echo can be seen as the direct reflection path, i.e., the contribution related to the path *transmitting antenna – interface – receiving antenna*. It is worth noting that this contribution keeps almost constant under

the assumption of a flat surface (as in the cases considered in the following), and thus it can be simply removed by a proper choice of the time window, which represents a key point for TG procedures.

In this work, the choice of the time window has been performed by following the simple geometric criterion proposed in [44]. Considering the sketch reported in Fig. 2 and indicating the y-coordinates of the generic receiver and transmitter of the array with y_r and y_t, respectively, with h the height of the array from the air-soil interface and with c the speed of light in the air, it is possible to define the TG instant $t_g(y_r - y_t)$ as

$$t_g\left(y_r - y_t\right) = t_{ts} + \alpha \cdot t_{sr}\left(y_r - y_t\right)$$

$$t_{ts} = \frac{2h}{c}$$

$$t_{sr}\left(y_r - y_t\right) = \frac{\sqrt{\left(y_r - y_t\right)^2 + 4h^2}}{c} \tag{9}$$

in which t_{ts} represents the time for the wave to travel, under the ray-trace approximation, from the transmitter to the soil, $t_{sr}(y_r - y_t)$ is the time required to cover the soil-receiver distance, and $\alpha \geq 1$ is a multiplicative constant. For the purposes of this article, a value $\alpha = 1.5$ was employed to select the duration of the window.

Therefore, the field at the receiver location y_r due to the transmitter in y_t after the application of the TG procedure is expressed as

$$\boldsymbol{e}_r^{TG}\left(y_r - y_t, t\right) = \begin{cases} \boldsymbol{e}_r\left(y_r - y_t, t\right), & t \geq t_g, \\ 0, & t < t_g, \end{cases} \tag{10}$$

in which $\boldsymbol{e}_r$ is the time-domain electric-field vector collected at the receiver location y_r when the source in y_t is active.

Another important step in the herein proposed preprocessing of the data is the background removal, which represents a well-known procedure in geophysics [1]. This procedure consists of taking as datum the difference between the current trace and the average value of a set of traces symmetrically centered around the current one. Thus, if the average is performed on $2N + 1$ traces whose spatial step between consecutive traces is Δs, the datum after time gating and background removal $\boldsymbol{e}_r^{TG,B}$ can be written as

$$\boldsymbol{e}_r^{TG,B}(y, t) = \boldsymbol{e}_r^{TG}(y, t) - \frac{1}{2N+1}\sum_{n=-N}^{N} \boldsymbol{e}_r^{TG}(y - n \cdot \Delta s, t). \tag{11}$$

Considering the incident field invariant along the horizontal coordinate, the contribution of the incident field in $\boldsymbol{e}_r^{TG}$ is approximately the same as the average over the $2N + 1$ traces, and so they erase each other in (11), providing an estimate of the field scattered by the buried objects.

A key aspect of this processing is related to the choice of the number of traces to be used for the average evaluation. In the following, a background removal strategy on all the traces has been employed since it erases the spurious interface generated by the abrupt muting of the TG procedure and also limits the contributions coming up from the interfaces/clutter buried below

TABLE I
BURIED TARGET LOCATIONS AND ESTIMATED POSITIONS (DISTANCE OF THE OBJECT TOP SURFACE FROM THE GROUND)

TARGET	TRUE LOCATION [cm]	ESTIMATED POSITION [cm]
AT-1 (TMA-5)	12.0	12.0
AT-2 (VS-1.6)	11.5	11.3
AT-3 (VS-2.2)	13.0	13.1
AP-1 (TS-50)	1.5	1.4
AP-2 (TS-50)	1.5	1.7
AP-3 (TS-50)	2.0	1.2
AP-4 (mine simulant)	2.0	1.9
AP-5 (TS-50)	1.5	1.4
AP-6 (PFM1)	2.0	1.9
AP-7 (M-14)	1.5	Not detected
CL-1 (Nylon cylinder)	10.5	11.0
CL-2 (Aluminum sphere)	11.5	Not detected

the objects. Finally, the data is moved back to the frequency domain and processed by the imaging approach.

B. Landmines Data Set

A first experimental data set is composed of different targets which include metal spheres and a variety of anti-tank (AT) and anti-personnel (AP) dielectric mines of different sizes. Target depths range from a few centimeters up to 30 cm and the distance is to be intended from the surface of the sand to the top of the target. The ground medium is a damp, compacted sandy soil. Fig. 10 shows a picture of the targets involved in the scenario under test and their spatial locations and depths. Both plastic AT as well as AP mines are present, together with other various objects.

In order to evaluate the quality of GPR recoveries, Fig. 11(b) reports a 3D estimate of the buried target support via exploiting sparse multifrequency BA method (i.e., (4) solved via ISTA), while Fig. 11(a) shows its reference. Regarding the frequency selection, 45 equally spaced frequencies in the range [0.8–4] GHz were employed. Note that, the highest frequencies are processed as they are not useful due to the attenuation in the soil. Fig. 11(b) shows the iso-surfaces of target supports and the colored slices representing the projections on each plane. For the sake of clarity, some slices of the retrieved profiles are reported in Fig. 12, and targets depths, both true and estimated ones, were reported in Table I.

As claimed in the previous sections, since we are interested in target support, one can assume the contrast constant with respect

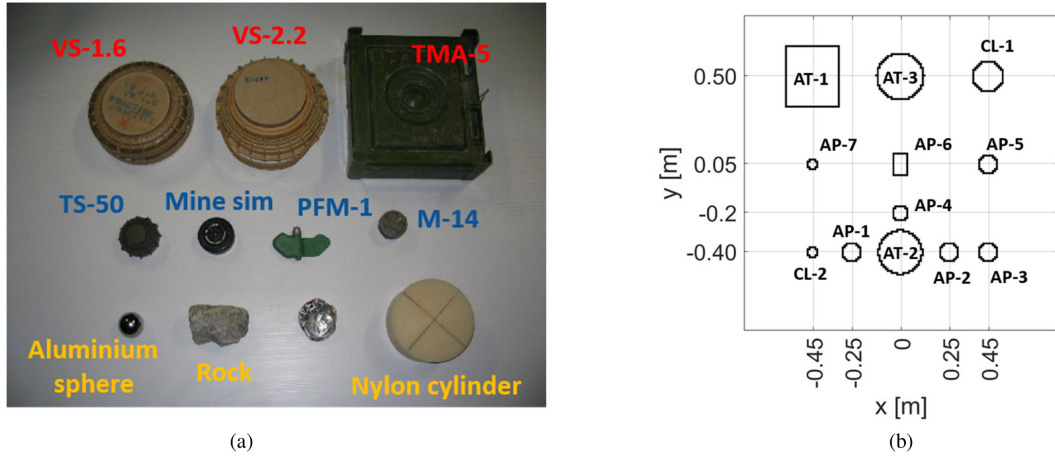(a)   (b)

Fig. 10.   Targets employed for the mine data sets (a) and their spatial locations (b). The objects in red refer to AT plastic mines, the blue ones to anti-personnel AP mines and the dark yellow ones refer to other objects. The depths of the buried targets are: AT-1 (TMA-5): 12 cm, AT-2 (VS-1.6): 11.5 cm, AT-3 (VS-2.2): 13 cm, AP-1 (TS-50): 1.5 cm, AP-2 (TS-50): 1.5 cm, AP-3 (TS-50): 2 cm, AP-4 (Mine simulant): 2 cm, AP-5 (TS-50): 1.5 cm, AP-6 (PFM1): 2 cm, AP-7 (M-14): 1.5 cm, CL-1 (Nylon cylinder): 10.5 cm, CL-2 (Aluminum sphere): 11.5 cm.

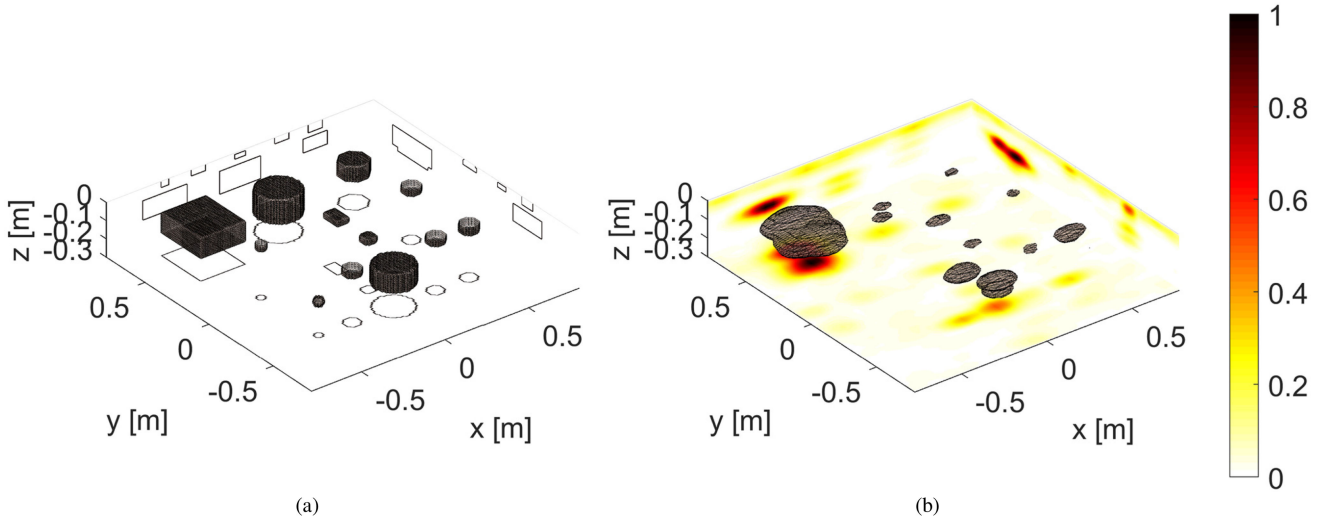(a)   (b)

Fig. 11.   Reference scenario with AT and AP plastic mines and other clutter objects (a) and its recovery via multi-frequency sparse BA approach (b). These results were obtained by processing 45 equally spaced frequencies in the range [0.8, 4] GHz.

(a)   (b)
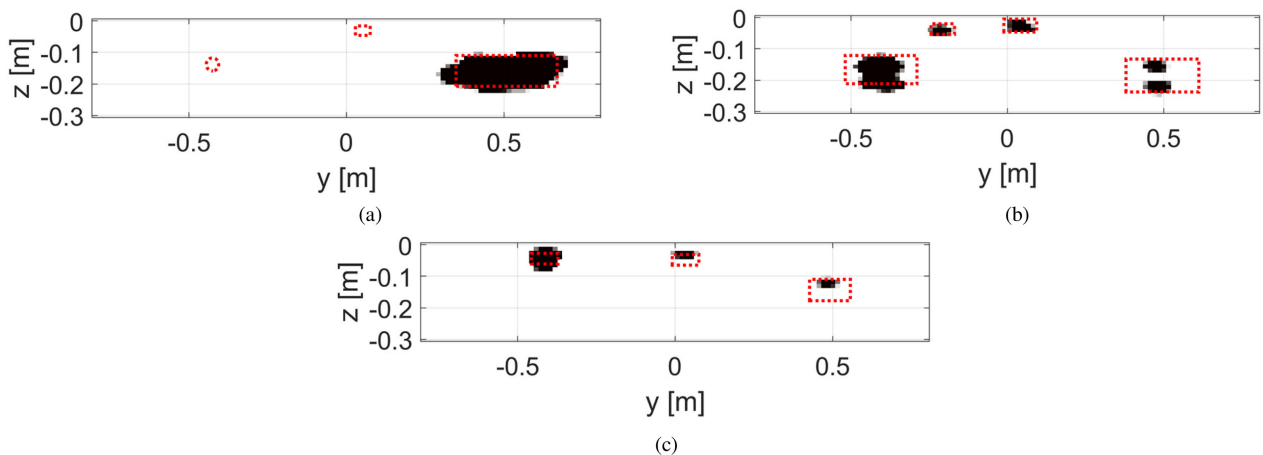

(c)

Fig. 12.   Some slices of retrieved objects supports (i.e., black areas) of Fig. 11(b): slices at (a) $x = -0.45$ m, (b) $x = 0$ m, (c) $x = +0.45$ m.
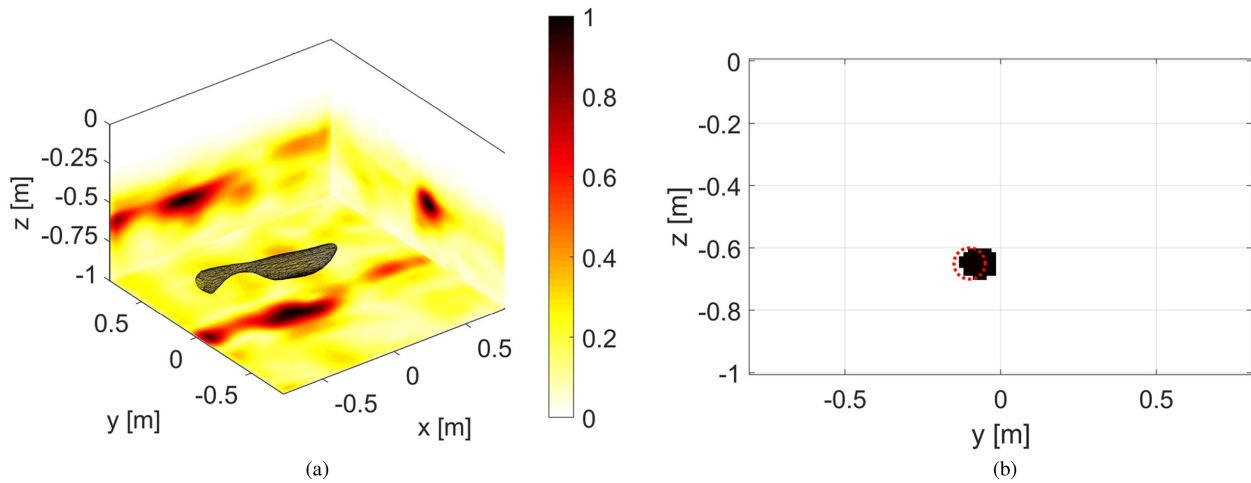
Fig. 13. Support recovery of a 10-cm-diameter plastic pipe buried at 58 cm (a) and its cross-section recovery at $x = -50$ cm (b). A picture of the reference is reported in [8].

to the frequency, thus reducing the computational burden and memory requirement for the recovery procedure. It is worth to note that the inversion was carried out via a 2.5D procedure, i.e., the GPR data corresponding to each slice are processed via a 2D algorithm, and then each reconstructed slice along the *x*-axis is merged with the others to cover the whole imaging domain.

The investigated area is discretized into $33 \times 108 \times 24$ voxels and all the slices were normalized by the largest magnitude in the whole 3D image. As expected, larger targets with higher contrasts have stronger responses: indeed, the TMA-5 AT plastic mine has a bigger retrieved support rather than other objects like the VS-1.6 and VS-2.2, notwithstanding their size. The strong contribution of the TMA-5 mine to the data might also justify the small recovery for the VS-2.2, which is worse than the one of the VS-1.6 despite their comparable size, and this might be related to its farther distance from the biggest objects in the domain. Regarding other objects such as the metal sphere and the M-14 AP plastic mine, they are not visible in Fig. 11(b) due to their small size, depth, and/or composition. For similar reasons, the big nylon cylinder is not properly imaged, since its dielectric permittivity is close to that of the soil.

It is important to note that with respect to the results in [9]–[12], the proposed processing allows us to better locate and estimate the target supports. More in detail, the approaches reported in [9] and [12], based on the average similarity function, are only able to retrieve targets locations projected on the air–soil interface, but no additional information is available regarding objects depths, and the retrieved images appear blurred. Conversely from the aforementioned articles, the work in [10] provides also the depth information but only for a 2D slice (i.e., the central one) and no other images are reported for the whole imaging region. Last, but not least, the work in [11] still provides alternative 2D sparse, data processing to the previous solutions, but computationally heavy and almost impracticable for real scenarios.

C. Buried Pipe

Another example is composed of a hollow 10-cm-diameter plastic pipe buried at 58 cm depth in the same sandy soil employed for the data set of landmines data set. The very accurate results of the recovery algorithm based on the use of the multifrequency BA method and ISTA with the same settings as described previously are reported in Fig. 13. The threshold exploited to create the iso-surface in the image was fixed at 0.5. Fig. 13 shows clearly the location and the size of the buried pipe, as proved in [8].

VII. CONCLUSION

In this article, for the first time, the authors have proposed an analysis of the recovery performance of the unconventional, contactless, MVMS GPR system designed at the Georgia Institute of Technology and tested tomographic approaches against it.

An energy-based performance indicator is defined as well as the spectral coverage of the single-frequency tomographic imaging operator is evaluated. Moreover, performance comparison with respect to the use of a full aperture system has been performed. The analysis has shown that the investigated area covered by the GT apparatus can be limited in the extension compared to the full aperture case, i.e., objects buried in the deeper and sider parts of the investigation area could be not properly imaged with respect to the ones located in the center. The worsening in the recovery performance is mainly related to the lower amount of collected data. However, this limitation can still be overcome via multifrequency data processing.

Before processing the experimental GT dataset, a numerical analysis has been performed by mimicking the system at hand and by exploiting two different tomographic linear approaches, i.e., LSM and BA method, this latter enhanced with CS theory. Between the two approaches, BA method has shown to be more effective due to the simultaneous processing of all the multifrequency information, as opposite to the LSM case, which instead

involves an *a-posteriori* combination of the single-frequency indicators.

Then, the experimental data have been processed by means of the combined use of multifrequency BA approximation and CS theory. In order to improve the preprocessing of the data, the two standard procedures of time gating and background removal have been employed together to filter out the air–soil interface contribution in the radargram as well as to handle the clutter.

Two different data sets have been processed: first including AT and AP plastic landmines and second one including a 4-inch buried pipe. In both scenarios, the proposed processing has been proved to be effective and extremely accurate to detect and locate the buried objects. These results have confirmed the better reconstruction capability of tomographic approaches if compared with the methods adopted in [9]–[12].

REFERENCES

[1] R. Persico, *Introduction to Ground Penetrating Radar: Inverse Scattering and Data Processing*. New York, NY, USA: Wiley, 2014.

[2] G. Ludeno, G. Gennarelli, S. Lambot, F. Soldovieri, and I. Catapano, "A comparison of linear inverse scattering models for contactless GPR imaging," *IEEE Trans. Geosci. Remote Sens.*, vol. 58, no. 10, pp. 7305–7316, Oct. 2020.

[3] D. Comite, A. Galli, I. Catapano, and F. Soldovieri, "Advanced imaging for down-looking contactless GPR systems," in *Proc. Int. Appl. Comput. Electromagn. Soc. Symp.*, 2017, pp. 1–2.

[4] R. Persico, "On the role of measurement configuration in contactless GPR data processing by means of linear inverse scattering," *IEEE Trans. Antennas Propag.*, vol. 54, no. 7, pp. 2062–2071, Jul. 2006.

[5] X. Feng and M. Sato, "Pre-stack migration applied to GPR for land mine detection," *Inverse Problems*, vol. 20, no. 6, pp. S99–S115, Dec. 2004.

[6] C. J. Leuschen and R. G. Plumb, "A matched-filter-based reverse-time migration algorithm for ground-penetrating radar data," *IEEE Trans. Geosci. Remote Sens.*, vol. 39, no. 5, pp. 929–936, May 2001.

[7] C. Fischer, A. Herschlein, M. Younis, and W. Wiesbeck, "Detection of antipersonnel mines by using the factorization method on multistatic ground-penetrating radar measurements," *IEEE Trans. Geosci. Remote Sens.*, vol. 45, no. 1, pp. 85–92, Jan. 2007.

[8] T. Counts, A. C. Gurbuz, W. R. Scott, J. H. McClellan, and K. Kim, "Multistatic ground-penetrating radar experiments," *IEEE Trans. Geosci. Remote Sens.*, vol. 45, no. 8, pp. 2544–2553, Aug. 2007.

[9] A. Gharamohammadi and A. Shokouhmand, "A robust whitening algorithm to identify buried objects with similar attributes in correlation-based detection," *J. Appl. Geophys.*, vol. 172, 2020, Art. no. 103917.

[10] H. Zhang, O. Shan, G. Wang, J. Li, S. Wu, and F. Zhang, "Back-projection algorithm based on self-correlation for ground-penetrating radar imaging," *J. Appl. Remote Sens.*, vol. 9, no. 1, Jul. 2015, Art. no. 095059.

[11] K. R. Krueger, J. H. McClellan, and W. R. Scott, "Efficient algorithm design for GPR imaging of landmines," *IEEE Trans. Geosci. Remote Sens.*, vol. 53, no. 7, pp. 4010–4021, Jul. 2015.

[12] A. Gharamohammadi, F. Behnia, and R. Amiri, "Imaging based on correlation function for buried objects identification," *IEEE Sensors J.*, vol. 18, no. 18, pp. 7407–7413, Sep. 2018.

[13] M. Ambrosanio, M. T. Bevacqua, T. Isernia, and V. Pascazio, "The tomographic approach to ground-penetrating radar for underground exploration and monitoring: A more user-friendly and unconventional method for subsurface investigation," *IEEE Signal Process. Mag.*, vol. 36, no. 4, pp. 62–73, Jul. 2019.

[14] M. Pastorino, *Microwave Imaging*. New York, NY, USA: Wiley, May 2010.

[15] I. Catapano, F. Soldovieri, and L. Crocco, "On the feasibility of the linear sampling method for 3D GPR surveys," *Prog. Electromagn. Res.*, vol. 118, pp. 185–203, 2011.

[16] R. Persico, R. Bernini, and F. Soldovieri, "The role of the measurement configuration in inverse scattering from buried objects under the born approximation," *IEEE Trans. Antennas Propag.*, vol. 53, no. 6, pp. 1875–1887, Jun. 2005.

[17] D. Colton, H. Haddar, and M. Piana, "The linear sampling method in inverse electromagnetic scattering theory," *Inverse Problems*, vol. 19, no. 6, 2003, Art. no. S105.

[18] I. Catapano, L. Crocco, and T. Isernia, "Improved sampling methods for shape reconstruction of 3-D buried targets," *IEEE Trans. Geosci. Remote Sens.*, vol. 46, no. 10, pp. 3265–3273, Oct. 2008.

[19] L. L. Monte, D. Erricolo, F. Soldovieri, and M. C. Wicks, "Radio frequency tomography for tunnel detection," *IEEE Trans. Geosci. Remote Sens.*, vol. 48, no. 3, pp. 1128–1137, Mar. 2010.

[20] D. Donoho, "Compressed sensing," *IEEE Trans. Inf. Theory*, vol. 52, no. 4, pp. 1289–1306, Apr. 2006.

[21] I. Daubechies, M. Defrise, and C. D. Mol, "An iterative thresholding algorithm for linear inverse problems with a sparsity constraint," *Commun. Pure Appl. Math.*, vol. 57, no. 11, pp. 1413–1457, Nov. 2004.

[22] M. Ambrosanio, R. Autieri, and V. Pascazio, "A compressive sensing based approach for microwave tomography and GPR applications," in *Proc. IEEE Geosci. Remote Sens. Symp.*, 2014, pp. 3144–3147.

[23] R. Persico, S. Negri, F. Soldovieri, and E. Pettinelli, "Pseudo 3D imaging of dielectric and magnetic anomalies from GPR data," *Int. J. Geophys.*, vol. 2012, 2012, Art. no. 512789.

[24] I. Catapano, A. Affinito, G. Gennarelli, F. di Maio, A. Loperte, and F. Soldovieri, "Full three-dimensional imaging via ground penetrating radar: Assessment in controlled conditions and on field for archaeological prospecting," *Appl. Phys. A*, vol. 115, no. 4, pp. 1415–1422, 2014.

[25] W. C. Chew, *Waves and Fields in Inhomogeneous Media*. Piscataway, NJ, USA: IEEE Press, 1995.

[26] M. Bertero and P. Boccacci, *Introduction to Inverse Problems in Imaging*. Bristol, UK: Inst. Phys., 1998.

[27] O. M. Bucci, L. Crocco, T. Isernia, and V. Pascazio, "Subsurface inverse scattering problems: Quantifying, qualifying, and achieving the available information," *IEEE Trans. Geosci. Remote Sens.*, vol. 39, no. 11, pp. 2527–2538, Nov. 2001.

[28] K. Kim and W. R. Scott Jr., "A resistive linear antenna for ground-penetrating radars," *Proc. SPIE*, vol. 5415, pp. 359–370, Sep. 2004.

[29] M. Ambrosanio, M. T. Bevacqua, T. Isernia, and V. Pascazio, "Experimental multistatic imaging VIA the linear sampling method," in *Proc. IEEE Int. Geosci. Remote Sens. Symp.*, 2019, pp. 3586–3589.

[30] M. T. Bevacqua and T. Isernia, "Boundary indicator for aspect limited sensing of hidden dielectric objects," *IEEE Geosci. Remote Sens. Lett.*, vol. 15, no. 6, pp. 838–842, Jun. 2018.

[31] C. Estatico, A. Fedeli, M. Pastorino, and A. Randazzo, "A multifrequency inexact-newton method in L^p banach spaces for buried objects detection," *IEEE Trans. Antennas Propag.*, vol. 63, no. 9, pp. 4198–4204, Sept. 2015.

[32] S. Sun, B. J. Kooij, and A. G. Yarovoy, "Linearized 3-D electromagnetic contrast source inversion and its applications to half-space configurations," *IEEE Trans. Geosci. Remote Sens.*, vol. 55, no. 6, pp. 3475–3487, Jun. 2017.

[33] A. M. Alani *et al.*, "The use of ground penetrating radar and microwave tomography for the detection of decay and cavities in tree trunks," *Remote Sens.*, vol. 11, 2019, Art. no. 2073.

[34] Z. Zeng, J. Li, L. Huang, X. Feng, and F. Liu, "Improving target detection accuracy based on multipolarization MIMO GPR," *IEEE Trans. Geosci. Remote Sens.*, vol. 53, no. 1, pp. 15–24, Jan. 2015.

[35] M. A. González-Huici, I. Catapano, and F. Soldovieri, "A comparative study of GPR reconstruction approaches for landmine detection," *IEEE J. Sel. Topics Appl. Earth Observ. Remote Sens.*, vol. 7, no. 12, pp. 4869–4878, Dec. 2014.

[36] P. C. Hansen, "The discrete picard condition for discrete ill-posed problems," *BIT Num. Math.*, vol. 30, pp. 658–672, 1990.

[37] P. C. Hansen and D. P. O'Leary, "The use of L-curve in the regularization of discrete ill-posed problem," *SIAM J. Sci. Comput.*, vol. 14, no. 6, pp. 1487–1503, Nov. 1993.

[38] A. Beck and M. Teboulle, "A fast iterative shrinkage-thresholding algorithm for linear inverse problems," *SIAM J. Imag. Sci.*, vol. 2, no. 1, pp. 183–202, 2009.

[39] 2020. [Online]. Available: https://waymond-scott.ece.gatech.edu/multistaticbeamformingdata/multistaticbeamformingdata/

[40] L. L. Monte, D. Erricolo, F. Soldovieri, and M. C. Wicks, "Radio frequency tomography for tunnel detection," *IEEE Trans. Geosci. Remote Sens.*, vol. 48, no. 3, pp. 1128–1137, Mar. 2010.

[41] E. Cristofani, M. Becquaert, S. Lambot, M. Vandewal, J. Stiens, and N. Deligiannis, "Random subsampling and data preconditioning for ground penetrating radars," *IEEE Access*, vol. 6, pp. 26866–26880, 2018.

[42] O. Cmielewski, H. Tortel, A. Litman, and M. Saillard, "A two-step procedure for characterizing obstacles under a rough surface from bistatic measurements," *IEEE Trans. Geosci. Remote Sens.*, vol. 45, no. 9, pp. 2850–2858, Sep. 2007.

[43] E. Temlioglu and I. Erer, "Clutter removal in ground-penetrating radar images using morphological component analysis," *IEEE Geosci. Remote Sens. Lett.*, vol. 13, no. 12, pp. 1802–1806, Dec. 2016.

[44] R. Solimene, A. D' Alterio, and F. Soldovieri, "Half-space estimation by time gating based strategy," in *Proc. 13th Int. Conf. Ground Penetrating Radar*, 2010, pp. 1–5.

[45] R. Solimene, A. Cuccaro, A. Dell'Aversano, I. Catapano, and F. Soldovieri, "Ground clutter removal in GPR surveys," *IEEE J. Sel. Topics Appl. Earth Observ. Remote Sens.*, vol. 7, no. 3, pp. 792–798, Mar. 2014.

Michele Ambrosanio (Member, IEEE) was born in Naples, Italy, in 1987. He received the B.S. and M.S. degrees (summa cum laude) in biomedical engineering from the University of Naples "Federico II," Naples, Italy, in 2009 and 2012, respectively, and the Ph.D. degree in information engineering from the University of Naples "Parthenope," Naples, Italy in 2016.

He was a visiting Ph.D. student with the School of Natural and Mathematical Sciences, King's college, London from April to July 2015, and was with Mediwise Ltd. from July to November 2015, working on biomedical applications of microwave imaging for diagnostic purposes in the framework of his Ph.D. program. He is currently working as Postdoctoral Researcher with the University of Naples Parthenope. His research interests include electromagnetic inverse scattering problems for noninvasive diagnostics, ground penetrating radar, and biomedical applications of microwave imaging

Dr. Ambrosanio is a member of COST Action MiMed (TD1301), "Development of a European-based Collaborative Network to Accelerate Technological, Clinical and Commercialisation Progress in the Area of Medical Microwave Imaging", and COST Action TU1208, "Civil Engineering Applications of Ground Penetrating Radar."

Martina Teresa Bevacqua (Member, IEEE) was born in Reggio Calabria, Italy, in 1988. She received the M.S. Laurea degree (summa cum laude) in electronic engineering and the Ph.D in information engineering from the Università Mediterranea of Reggio Calabria, Reggio Calabria, Italy, in July 2012 and May 2016, respectively.

She is currently working as an Assistant Professor with the Università Mediterranea of Reggio di Calabria and her research activity mainly concerns electromagnetic inverse scattering problems with particular interest in biomedical and subsurface noninvasive diagnostics.

Dr. Bevacqua was the recipient of the Barzilai Award from the Italian Electromagnetics Society, in 2014 and Young Scientist Award during the 2018 URSI Atalantic Radio Science Meeting. Moreover, she received the Honorable Mention from IEEE-Antennas and Propagation Society (Central and Southern Italy Chapter) in the 2016 best student member paper competition.

Tommaso Isernia (Senior Member, IEEE) received the Laurea degree (summa cum laude) and the Ph.D. degree from the University of Naples Federico II, Naples, Italy, in 1988 and 1992, respectively.

He is currently a Full Professor of electromagnetic fields and Chair of the Department of Information Engineering, Infrastructures and Sustainable Energy with the Università Mediterranea of Reggio Calabria, Reggio Calabria, Italy. Moreover, he serves as the Supervisor with the LEMMA Research Group and the Ph.D. course on information engineering. He is currently with the Consorzio Nazionale Italiano per le Telecomunicazioni Consortium. He is also involved in the field of synthesis problems for biomedical imaging and therapeutic applications. His current research interests include inverse problems in electromagnetics, particularly emphasis on phase retrieval, inverse scattering, and antenna synthesis problems.

Dr. Isernia was a recipient of the G. Barzilai Award from the Italian Electromagnetics Society, in 1994. He serves as a member on the Board of Administrators for Consorzio Nazionale Italiano per le Telecomunicazioni Consortium.

Vito Pascazio (Senior Member, IEEE) graduated summa cum laude in electronic engineering from the Università di Bari, Bari, Italy, in 1986. In 1990, he received the Ph.D. degree in electronic engineering and computer science from the Department of Electronic Engineering, Università di Napoli Federico II, Napoli, Italy.

Currently, he is a Full Professor and Chair of the Department of Engineering, Università di Napoli Parthenope, Napoli, Italy. In 1990, he was with the Research Institute on Electromagnetics and Electronic Devices, Italian National Council of Research, Napoli, Italy. From 1994 to 1995, he was a Visiting Scientist with the Laboratoire des Signaux et Systemes of the Ecole Superieure d' Electricite (Supelec), Gif sur Yvette, France, and from 1998 to 1999, with the Universite de Nice Sophia-Antipolis, Nice, France. He was also the Director of National Laboratory of Multi-Media Communications of the Italian Consortium of Telecommunications, Napoli, Italy. He has published more than 180 technical papers. His research interests include remote sensing, image processing, and linear and nonlinear estimation, with particular emphasis to image computing and processing, and reconstruction of microwave and radar images.

Dr. Pascazio was the recipient of the Philip Morris Prize for Scientific and Technological Research, in 1990. He was a General Co-Chairman of IGARSS-2015 conference.